# Optimization of Power Density by Local Gear Failure Modeling

Marco Kampka, Christian Brecher and Christoph Löpenhaus

## Introduction and Motivation

Power density is a key factor in gear design. Increasing the power density enables engineers to use smaller gears for their applications which lead to smaller and lighter gear boxes. The benefit for example for the automotive industry is less moving load in the vehicles and therefor a reduction of fuel consumption and subsequently a reduction of $CO_2$ emission. The limiting factor for the increase in power density of gears is the material strength in regard to the critical failure mode.

The most common way to design gears is using industry standards in which the material strength can be obtained either from fatigue limit tables, which are based on test rig results, or from the calculation of local material data (e.g. based on hardness, residual stress, and oxidation) by means of empirical formulae. Due to the limited empirical data, a lot of averaging and approximations are used to make the available standards applicable to a wide range of applications. To cover for the uncertainties due to this fact, the gears will be designed on the safe side and a near maximum power density will not be achieved.

To design the gear closer to the power density limit, a high level of information concerning the load carrying capacity for the specific failure mode is necessary. In this paper, the three major gear failure modes pitting, tooth root breakage and flank fracture will be discussed. Those failure modes have in common that they start with a local exceeding of the material strength in regard to their specific load situation. This paper will show how local FEA-based calculation approaches can be used to design gears closer to their power density limits for pitting, tooth root breakage and flank

fracture. The calculation results will be validated in running tests on different test rigs. The testing results will then be compared to the results of the local FEA-based calculation approaches as well as to the common industry standard ISO 6336.

Increasing the power density of gears is always a major goal in gear design. Transmitting higher power with smaller gears decreases the size of the gearbox itself and gives more room for other devices or components. At the same time, the downsizing reduces weight. In an automotive transmission this will lead to a higher fuel efficiency and less $CO_2$ emission. The required high power density of the gearbox demands an exact calculation method for the strength against the predominant failure modes of the given gear sets. This includes pitting, tooth root breakage and flank fracture. The precise recalculation of the tooth strength is necessary, as the downsizing leads to a reduction of the remaining safety reserves.

With regards to the calculation of the strength of cylindrical gears, a trend towards local calculation approaches

is visible. Instead of calculations solely based on standards and global calculation approaches, local approaches based on finite element analysis (FEA) are used. A big advantage of FEA and FE-based tooth contact analysis (FE-TCA), respectively, is the consideration of the exact geometry including flank modifications, the local stiffness behavior, and thus, the precise calculation of forces and stresses. In contrast, global approaches are based on simplified models and phenomenological formulas (Fig. 1).

In the end, the capabilities of both standard calculations and FE methods are limited. The applicability of standards for gears similar to the test data base is very good. Arbitrary gear size, gear geometry, material properties or surface properties may cause issues. For example, larger gears require higher safety factors, whereas smaller gears demand lower safety factors for a correct prediction of strength (Refs. 1–2).

FE methods, however, are also limited with regards to the prediction of the load carrying capacity of gears. Reasons are the dependency of the results upon the
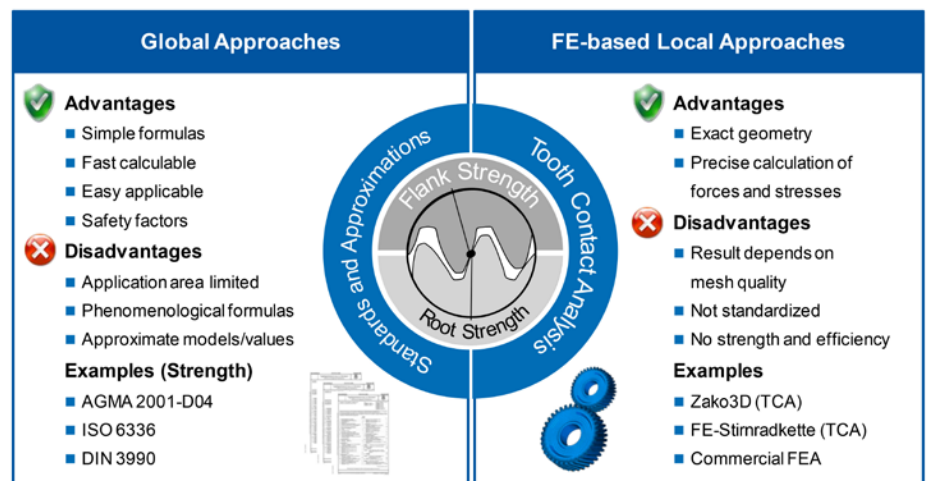


**Figure 1    Calculative approaches for flank strength.**

mesh characteristics, e.g. — density and uniformity, and missing or simplifying local models and properties, e.g. — friction coefficients and material parameters. Though the loads and stresses can be calculated very precisely, especially considering flank modifications, the prediction of strength is not a common result of today's FE-TCA.

## Objective and Approach

The main failure modes of gears are pitting, tooth root breakage and flank fracture. During the design stage existing (ISO 6336-2, 6336-3, AGMA 2001) and proposed (ISO/DTS 6336-4) standards can be used to check designs regarding those failure modes (Refs. 3–6). Since those standards use simplified approaches to calculate the loads and compare them to empirical strength data and due to the nature of standards using conservative estimates, the load carrying capacity limits of the components are most likely not reached. Therefore, potential to increase power density will not be used fully.

One alternative is to use FE approaches. While the composition of stresses and the location of failure initiation are very different, the fatigue failure modes pitting, tooth root breakage and flank fracture have in common that they are all initiated by a local exceeding of the material strength. The material in general is not ideally homogeneous. Each material will, to a certain degree, consist of imperfections that include pores or inclusions. Those imperfections will cause premature failure by crack initiation due to a local stress maximum because of the variation of Young's modulus. This is taken into account by local strength calculation approaches using weakest link models (Fig. 2). During the FE-simulation a probability of failure/survival is calculated for each volume element. The multiplication of the single probabilities will result in the total probability of the calculated failure for the whole component.

This paper will introduce FE-based local calculation methods to predict the failure modes pitting, tooth root breakage and flank fracture. For each failure mode, the special adaption of the calculation methods will
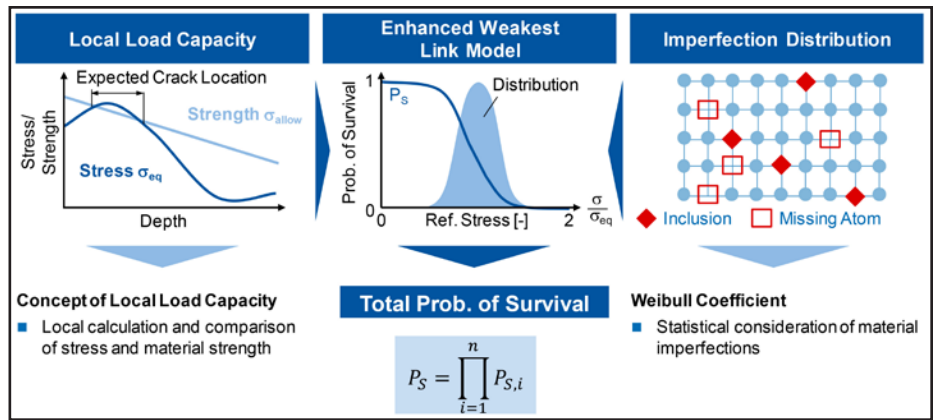


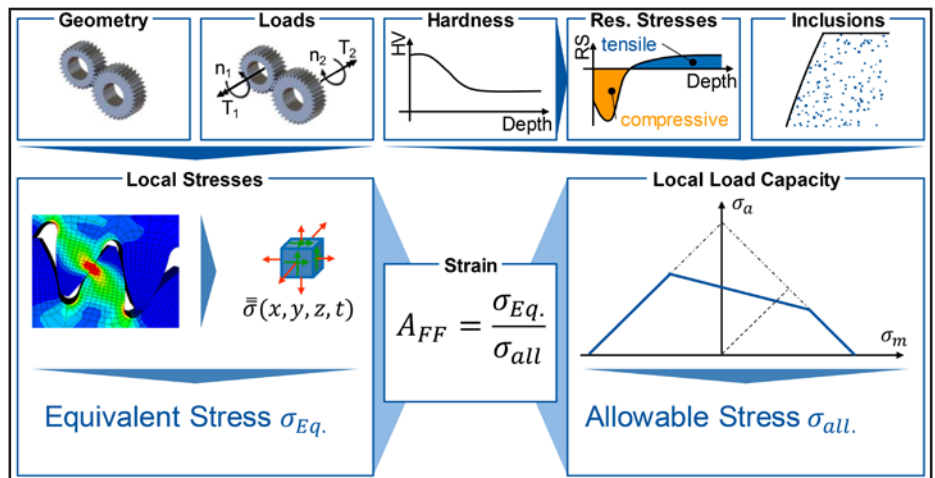Figure 2    Calculation approach in enhanced weakest link model.

$$P_S = \prod_{i=1}^{n} P_{S,i}$$



Figure 3    Local strength calculation approach.

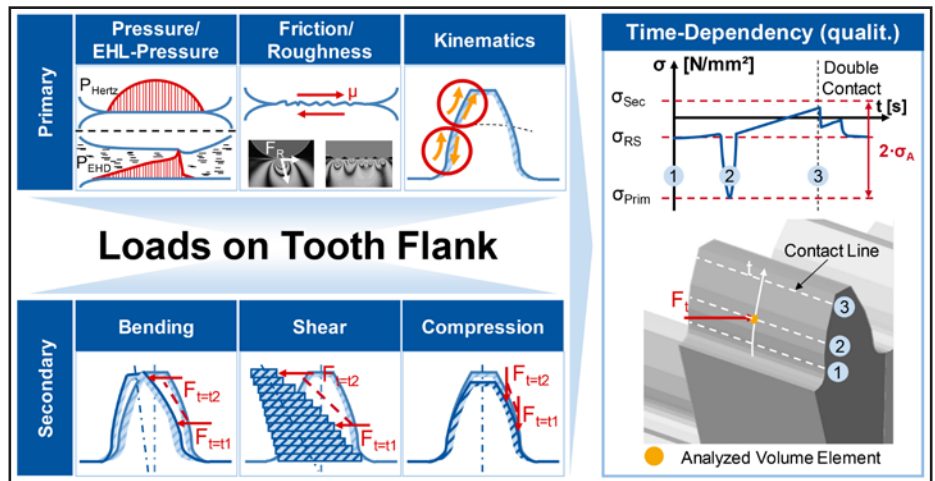$$A_{FF} = \frac{\sigma_{Eq.}}{\sigma_{all}}$$



Figure 4    Time-dependency of tooth flank stresses (Ref. 7).

be demonstrated. Subsequently, the results of the FE-based methods will be validated by test bench trials and compared to the ISO 6336 standard.

## Local Gear Failure Models

The basic input data needed to use a FE-TCA, regardless of the failure mode, is listed in the upper half of Figure 3. To calculate the local stresses the geometry of the gears and knowledge of the loads and kinematics is needed. The time-dependent stress calculation is carried out by means of FEA. The resulting stresses out of the FEA are then combined to an equivalent stress using different stress hypotheses depending on the fatigue failure mode. Those locally calculated equivalent stresses will be compared to the local load capacity of the stressed

element. The local load capacity is derived from the hardness and residual stress profile, the chosen material model and the characterization of the material imperfections in form of inclusions. If the local equivalent stress succeeds the allowable stress, failure will occur.

***Pitting.*** The torque transmission by gears is characterized by locally variable contact conditions on the tooth flank. Therefore, for each contact point the local loads have to be calculated. Direct results of FE-TCA are the local normal forces $F_N$, the sliding velocities $v_g$ and the normal force asymmetry factor $\lambda$ (kinematics). The stress cycle that an element on the tooth flank is exposed to during the contact can be divided into two different phases: primary and secondary loads (Fig. 4).

In the non-loaded conditions the residual stresses determine the entire state of stress (point 1). The initially applied primary loads result from the contact flattening due to the Hertzian contact and are characterized by a compressive state of stress that superimposes the residual stresses (Ref. 2). During the contact cycle the loads are characterized by normal, tangential and temperature stresses. After completing the load cycle, the considered volume element is exposed to an increasing tensile stress due to the deformation of the tooth. This part of the load sequence is called secondary load (Ref. 3). The secondary loads are determined by the amount of tangential and radial forces leading to bending, shear and compression states of stresses. The consideration of primary and secondary stresses can lead to an alternating stress state over the entire contact of a tooth pair. The resulting stress amplitudes are higher than just for the Hertzian contact and need to be considered in a strength model.

Besides the consideration of the exact stress state, the material strength has to be taken into account. For the calculation method, measured micro hardness and residual stress profiles are required. The material strength is described according to the conditions in Goodman's diagram that shows the permissible stress amplitude over the acting mean stress (Fig. 5). The approach is applied locally at each element.

The permissible stress amplitude is limited by the compressive/tensile yield strength $R'_{p0.2}$ on the one hand. On the other hand, the endurance strength is described over a huge interval of stress ratios $R$ by Goodman's straight. The level and gradient of the straight depends on the residual stress-free cyclic yield strength $\sigma_{W0}$ and the mean stress sensitivity $M$. Accordingly, compressive residual stresses that act as superimposed mean stresses lead to an increased permissible stress amplitude if the yield strength is not exceeded.

The used material model is fully adopted from Hertter (Ref. 8) despite the shown modifications (Fig. 5):
- Mean stress sensitivity is calculated acc. to LIU [9].
- Effective mean stress considers mean stress due to applied load in addition to mean stress due to residual stresses.
- Introduction of Weibull parameter for weakest link model.

The concept for the pitting strength calculation is shown (Fig. 6). The input data for the model consists of the contact geometry, external forces/torques and the material parameters. On this basis the probability of survival of the surface zone and the influenced bulk material is calculated. Based on the input data, a simplified analysis of the contact conditions takes place first. Therefore, the minimum relative film thickness in the contact is calculated. If a sufficient separation of surfaces is given $(\lambda = h_{0,th} / R_{q,mean} > 2)$ only the stresses in the volume are evaluated. Otherwise, a micro contact calculation is run in order to consider the stress peaks due to the contact of technical surfaces.

For the time-dependency of stresses (Fig. 4) the state of stress at each volume element is recorded over the entire mesh. Afterwards, the state of stress is compared locally to the material
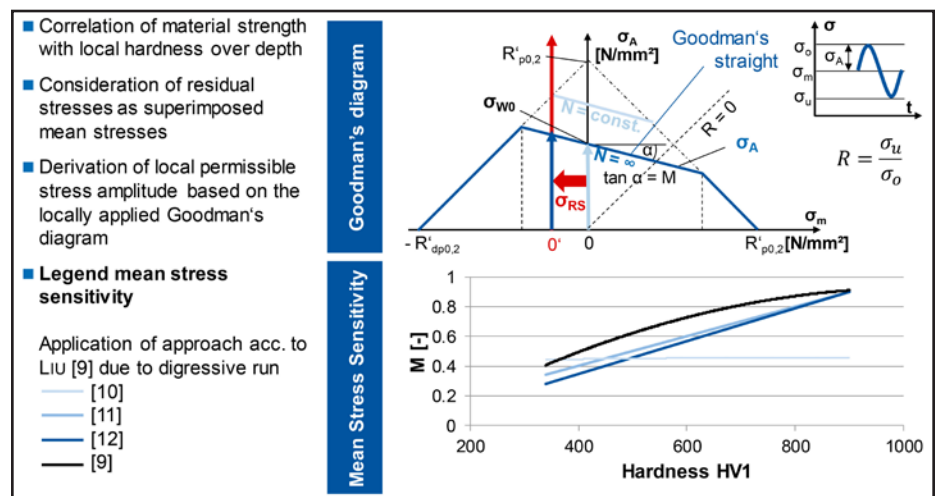


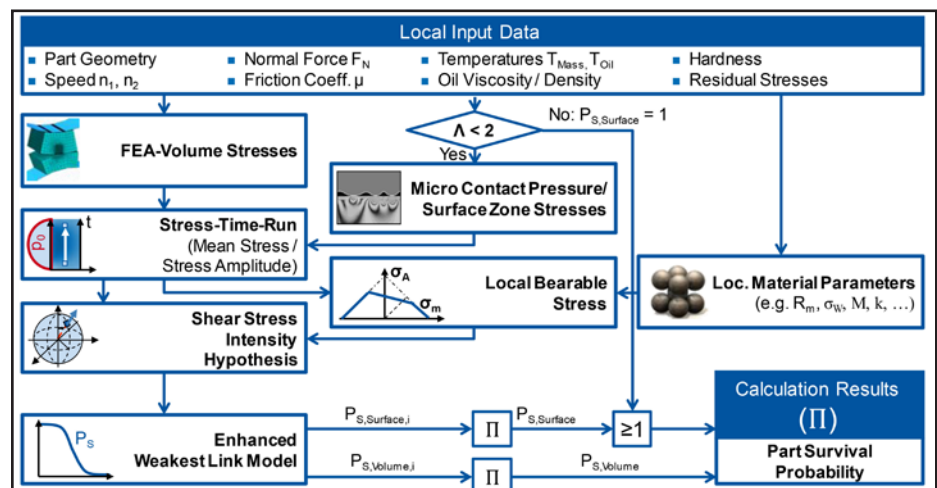Figure 5    Material strength in tooth flanks (Ref. 13).



Figure 6    Procedure for local pitting strength calculation (Ref. 7).

strength (Fig. 5). Therefore, the shear stress intensity hypothesis (SIH) acc. to Liu (Ref. 9) and modified by Hertter (Ref. 8) is used. The input parameters are now further enhanced by the mean stresses due to load, as well as residual stresses (Ref. 7). Therefore, the strains $A$ at each cross-section of a volume element are considered over the mesh in an integrative approach (Eqs. 1 and 2).

$$A(\gamma, \varphi) = \sqrt{\frac{a \cdot \tau_{\gamma\varphi,a}^2 (1 + m \cdot \tau_{\gamma\varphi,m}^2) + b\sigma_{\gamma\varphi,a}^2}{\sigma_A}} \quad (1)$$

$$A_{int,A} = \left\{ \frac{15}{8\pi} \int_{\gamma=0}^{\pi} \int_{\varphi=0}^{2\pi} [A(\gamma, \varphi)]^2 \cdot \sin\gamma \cdot d\varphi d\gamma \right\}^{\frac{1}{2}} \quad (2)$$

| | | |
|---|---|---|
| $A(\gamma,\varphi)$ | [-] | Strain of plane $(\gamma,\varphi)$ |
| $\tau_{\gamma\varphi,m}$ | [MPa] | Shear mean stress, plane $(\gamma,\varphi)$ |
| $\sigma_A$ | [MPa] | Permissible Stress Amplitude |
| $A_{int,A}$ | [MPa] | Entire strain of volume element |
| $\tau_{\gamma\varphi,a}$ | [MPa] | Shear stress amplitude, plane $(\gamma,\varphi)$ |
| $\sigma_{\gamma\varphi,a}$ | [MPa] | Normal stress amplitude, plane $(\gamma,\varphi)$ |
| $a,b,m,n$ | [div.] | Material Constants |

Finally, the probability of survival for each volume element at the surface and in the bulk volume is calculated according to the enhanced weakest link model that is applied on tooth flank contacts (Refs. 7 and 14). To parameterize the weakest link model, the local strain and local Weibull parameters are used. The total probability of survival of the component (final calculation result) is given by the product of all single probabilities of survival. This allows for the rating of an entire component with a single value by combining numerous local results (Eqs. 3 and 4).

$$P_{S,i} = 2^{-\frac{1}{V_0} \int_V A_i^{k_i} dV} \quad (3)$$

$$P_S = \prod_{i=1}^{n} P_{S,i} \quad (4)$$

| | | |
|---|---|---|
| $P_{S,i}$ | [-] | Probability of survival element $i$ |
| $A_i$ | [-] | Entire strain of element $i$ |
| $P_S$ | [-] | Probability of survival tooth flank |
| $V_0$ | [mm³] | Unity Volume |
| $k_i$ | [-] | Weibull's parameter element $i$ |

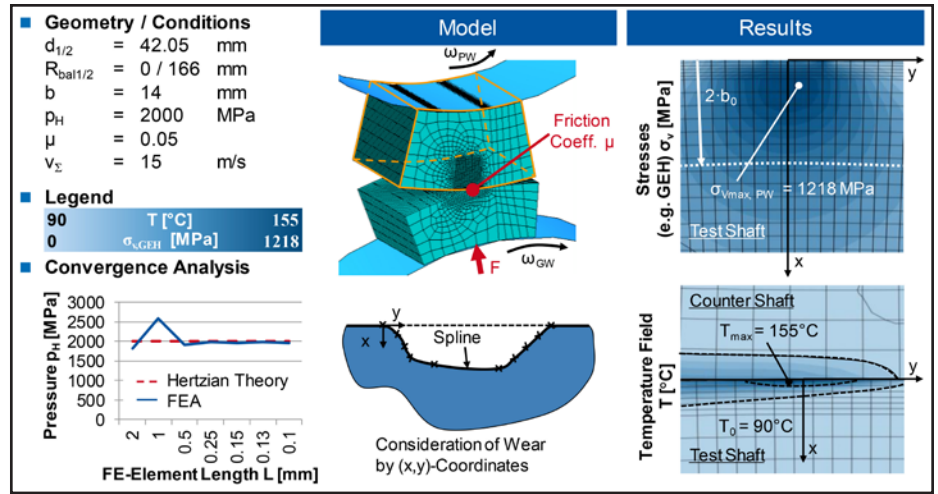In order to understand the general relations of influences and stresses in rolling-sliding contacts of gears, the contact conditions of simpler disk-on-disk-contacts have been analyzed first. The simulation of thermo-mechanic loads in the disk-on-disk-contact is done via FEA (Abaqus/CAE) (Ref. 7). In order to reduce the size of the FEA model, the test and counter shaft are represented by segments only (Fig. 7). For a further reduction of calculation time, the mesh density is locally increased in the contact area. The element type is C3D8T with a linear interpolative approach allowing fast calculation. The required mesh density in the contact area was evaluated by comparing the results of a convergence study of Hertzian pressure and with the ideal Hertzian contact theory. The maximum allowable element length found was $l_{FEA} = 250\,\mu m$. For temperature stresses at the very surface, the maximum allowable element length was $l_{FEA,T} = 50\,\mu m$.
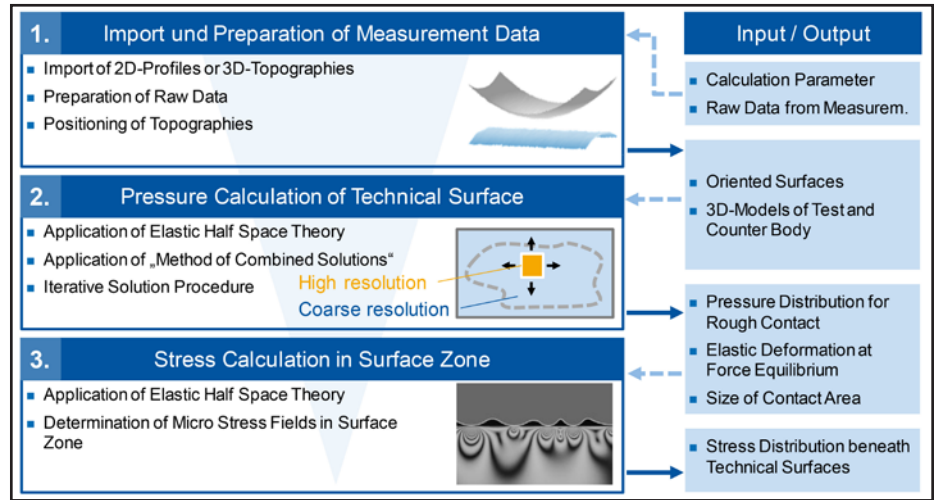
The FEA model allows the consideration of the most important influences on the stresses in the volume of the material due to normal, tangential, and thermal strains of the rolling-sliding contact under load. The values for geometry, normal forces, friction coefficient, and tangential velocities of test and counter shaft were derived from experimental measurements. As the wear of the contacting test parts changes the surface geometry and, consequently, the stress conditions in the subsurface region, a variable surface geometry has to be considered by a spline function. This was possible due to the fine mesh in the contact area.

The procedure for measurement-based surface stress field calculation is divided into three steps (Fig. 8). In a first step, measurement data is imported and modified for subsequent calculations.

Secondly, the pressure distribution under consideration of the technical surface geometry is calculated making



Figure 7    Subsurface stress model (Ref. 7).



Figure 8    Method for surface stress calculation (Refs. 7, 15).

use of the elastic half-space theory. Due to calculation performance, existing approaches are limited to small sections of the entire contact and use synthetic surface profiles. Therefore, the "Method of Combined Solutions" was developed that allows for contact calculations of large areas with high resolution (Ref. 15). With this method, non-conforming high-resolution grids are used in a specific area and a coarse resolution in all remaining areas. This allows for a detailed analysis of the contact conditions in the area of high resolution without neglecting the stiffness of the other areas of the contact. The area of high resolution is moved step by step over the entire contact area. For each configuration the calculation is repeated. At the end, all high-resolution solutions are combined. The result is a micro pressure distribution of the contact of technical surfaces. In a last step, the stress distribution below the

surface is calculated according to the pressure distribution from the second step. The stress distribution is again determined according to the half-space theory. This new contact calculation approach was successfully validated by a comparison of measured and simulated contact patterns and based on the values of the half-axes of the Hertzian contact ellipse.

In a last step the pitting strength calculation was validated. Therefore, a gear was designed to resemble the contact conditions of the disc-to-disc contact ($C$-$PT_{mod}$ according to (Ref. 16) modified with high lead crowning) (Fig. 9). This gear was used to investigate the fatigue strength on a back-to-back test rig. As expected, the high lead crowning results in a narrow centered contact pattern, as can be seen in the tests as well as in the FE-TCA. For each contact point on the tooth flank, the probability of survival was evaluated locally

(Fig. 9, top right). As expected, the minimum probability of survival occurs in the area of the damage origin. A major goal of the enhanced weakest link model is the consideration of the size effect in strength calculation. Hence, the model approach was applied on two additional test series from the literature (Ref. 17). The two test sets were in a comparable size range regarding the gear macro geometry as the variant (Fig. 9). Nevertheless, the lead crowning in the variants of (Ref. 17) was much, lower leading to a larger zone of applied stresses; consequently, a size influence is addressed. A representative damage and the distribution of probability of survival are shown (Fig. 9, bottom). The area of damage origin and minimum probability of survival are in congruence for this gear set as well.

In Figure 10 the torque levels for a probability of failure of 50% is shown. The same gear geometry 1 with a lead crowning of $C_{\beta2} = 121\,\mu m$ was used in the investigations. The test bench trials resulted in a torque level of $T_{inp,50\%} = 115\,Nm$. At the same time, the local calculation approach nearly matched that result and predicted a torque level of $T_{inp,50\%} = 123\,Nm$. However, the standard calculation according to ISO 6336-2 predicted a much higher tolerable input toque of $T_{inp,50\%} = 170\,Nm$. The reason for this is the basically non-existent consideration of modifications in the standard calculation. As shown before, the high lead crowning creates a narrow contact pattern that results in a higher Hertzian pressure, which subsequently results in an earlier failure due to contact fatigue. The local FE-based approach can take all modifications into account and, therefore, does not have the same limitations.

Gear geometry 2 was analyzed based on the results found in the literature (Ref. 17). The two investigated test series differed in heat treatment in terms of the case hardening depth chosen. Variant 1 had a case hardening depth of $CHD = 0.68\,mm$ which is equal to $0.14 \cdot m_n$, and therefore in the standard range of $0.1$–$0.2 \cdot m_n$. The case hardening depth of variant 2 was designed to be larger and out of the standard range. After heat treatment, a case hardening
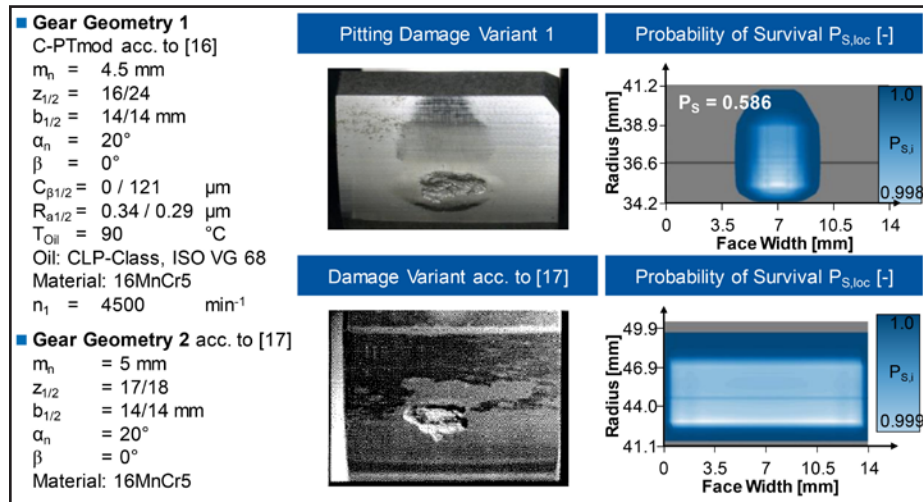


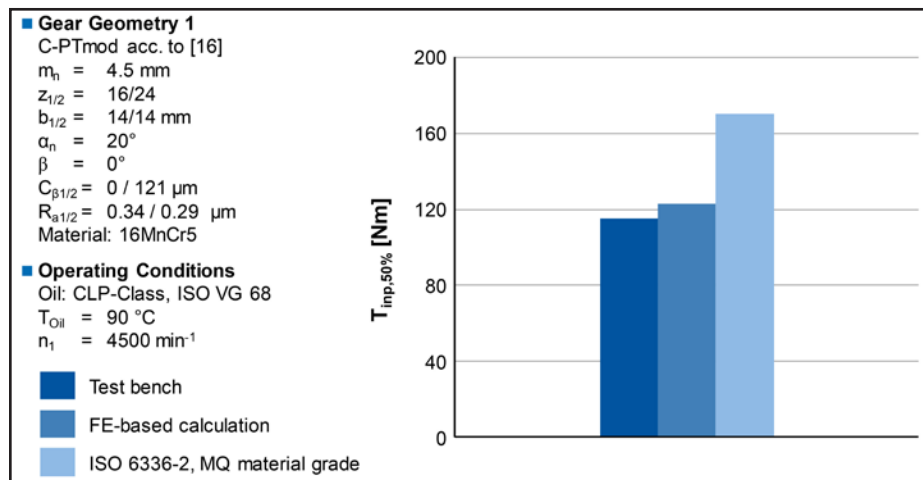**Figure 9    Transfer of local method onto tooth contact.**



**Figure 10    Comparison of calculated and tested fatigue strength ½.**

depth of $CHD = 1.46$ mm or $0.29 \cdot m_n$ was measured. In Figure 11, the test bench results are compared to the calculation results for the fatigue strength at 50% probability of failure. The calculations were carried out according to ISO 6336-2, using the average load capability of a MQ grade material and according to the FE-based approach described earlier in this section; the results were transformed to the corresponding torque levels. For heat treatment 1, the calculation according to ISO 6336-2 matches the tested load carrying capacity very well, whereas the simulation suggests a slightly lower load capacity. For heat treatment 2, the opposite is the case. This shows that the ISO 6336-2 standard is quite capable of predicting the gear load capacity for pitting if the gear geometry and material characteristics, e.g. — heat treatment parameters — are close to what was used to derive the standard itself. Outside of that range, a local FE-based approach is capable and more favorable to predict the load carrying capacity correctly.

***Tooth root breakage.*** Following the same principle, in evaluating the local strains and load capacities, the fatigue strength for tooth root breakage can be calculated. This approach was previously described in detail in (Ref. 25). This paper will include a short summary and add a comparison of the results to ISO 6336-3.

Since there is no surface-to-surface contact in the tooth root, the loads regarding Hertzian pressure, thermal loads, and micro Hertzian pressure due to rough surfaces can be ignored. The simplified model to calculate the tooth root load capacity is shown (Fig. 12).

In this report, two types of helical gears were investigated regarding tooth root breakage. The gear data of the two types is shown (Fig. 13). The main difference of the helical gears was the variation of the helix angle. The helix angle was set to $\beta = 20°$ and 33°. The normal module $m_n$ and the pressure angle $\alpha$ were constant for both helical gears. In order to match the center distance of $a = 91.5$ mm of the test bench, the number of teeth and the addendum modification factor of the gears were modified (Ref. 18).
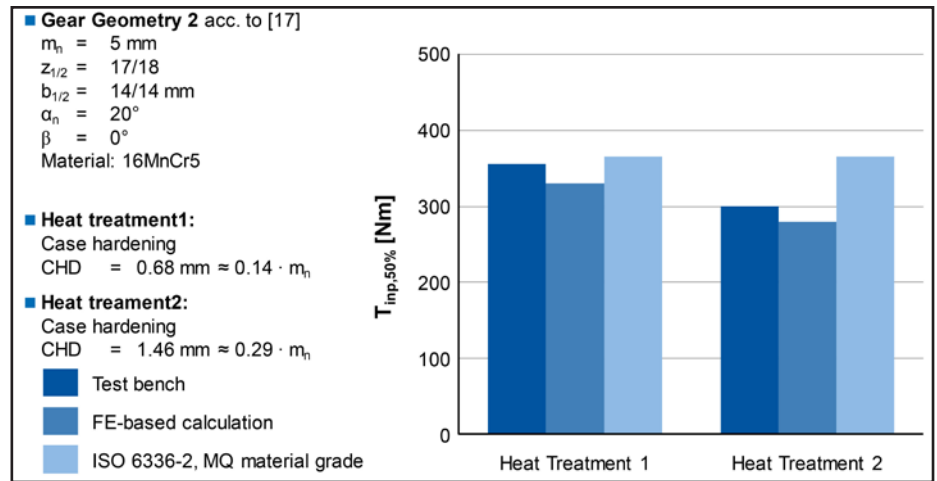


Figure 11    Comparison of calculated and tested fatigue strength 2/2.
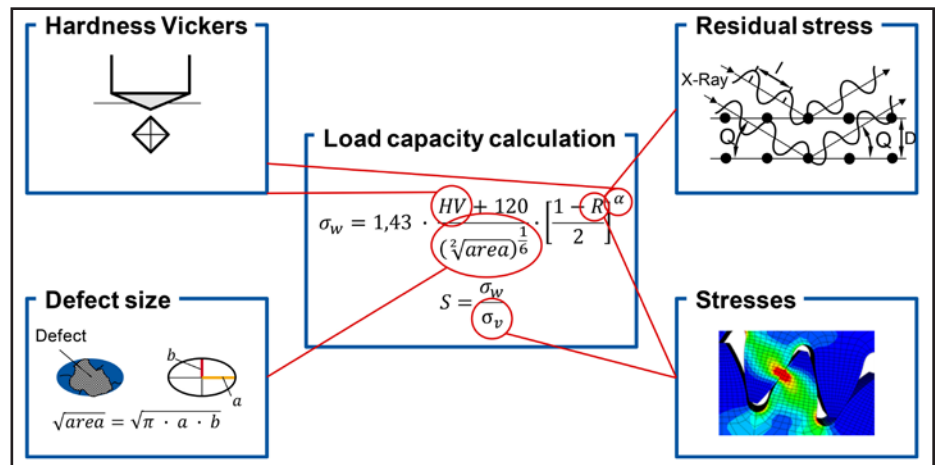


Figure 12    Influencing factors on the load carrying capacity of a defect (Ref. 18).
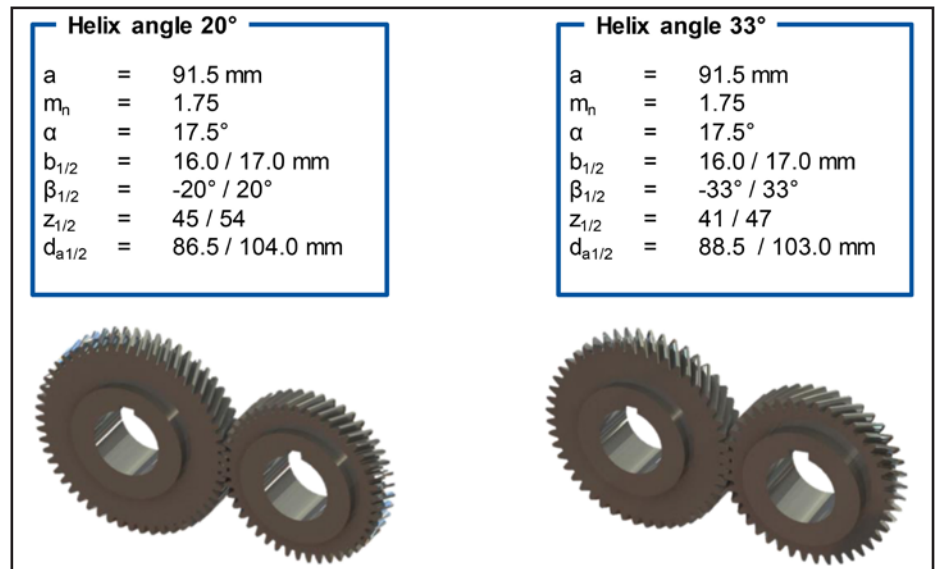


Figure 13    Evaluated gear macro geometries (Ref. 18).

Figure 14 depicts the material properties and defect distribution of the helical gears. The figure shows the Vickers hardness and the residual stresses on the right and the defects and there properties on the left side. The defect size was measured on fractured surfaces, and as the cumulative frequency indicates, it can be described by a Weibull-distribution (Ref. 18).

The comparison of the testing and simulation results for the sample helical gear with a helix angle of $\beta = 20°$ is shown (Fig. 15). The torque level that leads to a 50% probability of failure was evaluated based on the staircase method.

The average torque at the pinion was $T_{inp,50\%,test} = 502$ Nm for the eleven test runs, marked in black. The average torque at the pinion of the simulation was $T_{inp,50\%,sim} = 505$ Nm, marked in blue. The deviation of the two torque levels is less than 1%. The comparison of the results of the helical gear with a helix angle of $\beta = 20°$ shows a very high accordance of the simulation model and the testing results (Ref. 18). The results for both investigated macro geometries are summarized (Fig. 16). The calculation results based on the described FE-approach and ISO 6336-3 are compared to the test bench results.

For both sets, the deviation of the FE simulation and testing results is lower than 2%. It can be concluded that the proposed calculation method is capable of calculating the torque level that leads to a 50% probability of failure for a given gear (Ref. 18). The comparison to ISO 6336-3 shows that the gear with a helix angle of $\beta = 20°$ is represented well by the standard, whereas the load carrying behavior of the gear with a helix angle of $\beta = 33°$ could not be described. The ISO's scope is limited to a helix angle of $\beta = 25°$. Therefore, the ISO standard is not applicable to a higher helical angle, although those are very common, for example, in the automotive industry. The local FE-based method does not have these restrictions by design, and is not limited to an empiric database in terms of gear macro geometry. This enables the local FE-based approach to predict the gear load capacity correctly for arbitrary geometries.

*Flank fracture.* Flank fractures can occur on cylindrical and bevel gears (Refs. 19–20). These failures are breakages of teeth in the area of the active tooth flank. These fractures have their origin in the inner component volume, usually starting close to the pitch circle and showing a characteristic course of the primary crack of about 45° to the active tooth flank (Ref. 21). In addition to the primary crack, secondary and tertiary cracks are also observed
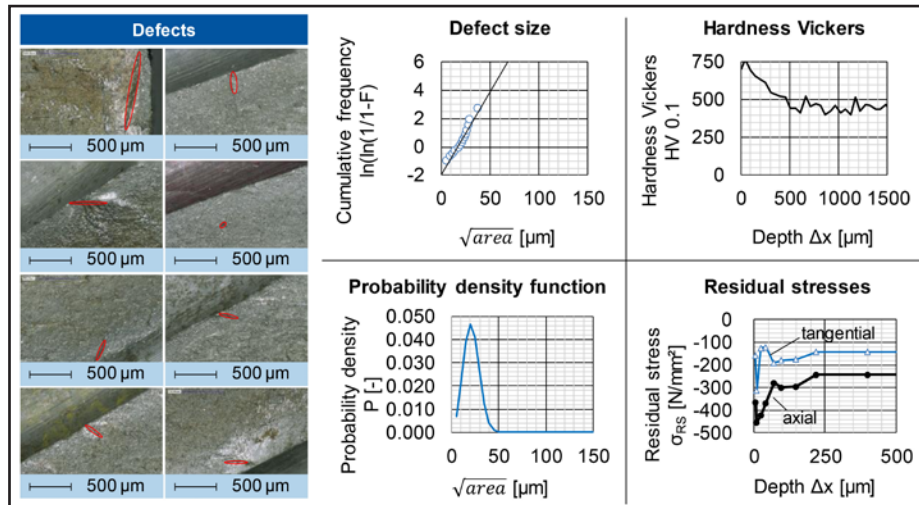


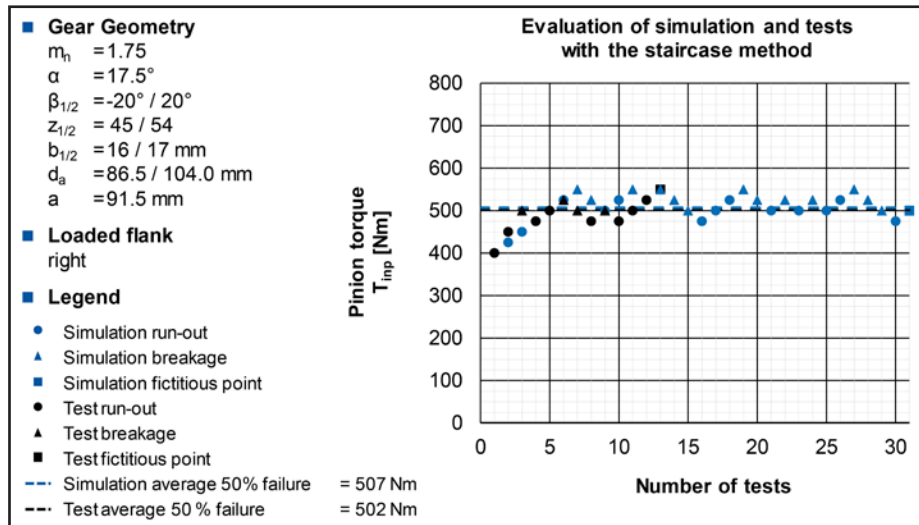Figure 14    Material and defect characterization (Ref. 18).



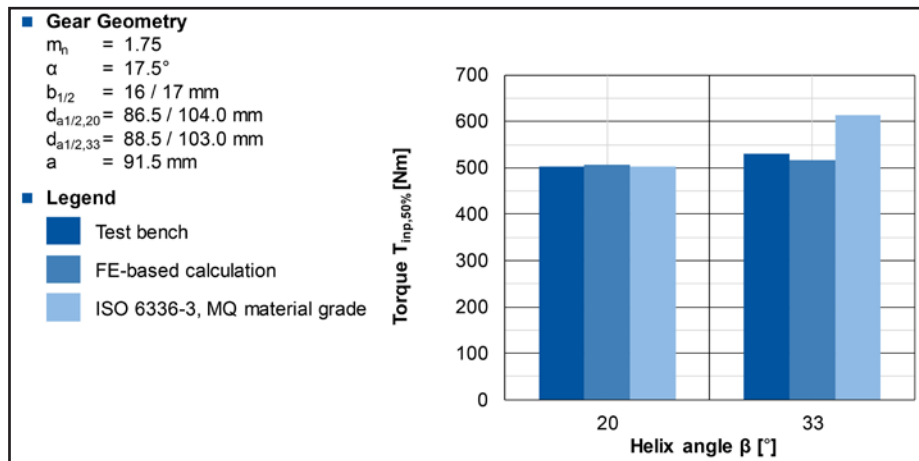Figure 15    Comparison of the simulation and testing results for the helical gears (Ref. 18).



Figure 16    Overall comparison of the simulation and testing results for all tested gears (Ref. 18).

in existing literature about tooth flank fracture. They arise due to the change in the local stiffness properties caused by the primary crack and run parallel to the tooth tip below the primary crack (Ref. 22). Flank fractures have their crack origin in the inner component volume at a depth that corresponds to about twice the case hardening depth. Often a defect in the structure is discovered at the crack origin. When using case hardening steel 18CrNiMo7-6, those defects mostly consist of aluminum oxides ($Al_2O_3$) and when using 20MnCr5 they mostly consist of manganese sulfide (MnS) (Ref. 22). The chemical composition of the defects is irrelevant. Rather, the difference in the Young's modulus between the defect and the steel matrix is considered to be the cause of a stress exaggeration at the defect and an associated crack initiation (Refs. 6 and 22). According to the current flank fracture model that resulted in ISO/DTS 6336-4, the Hertzian pressure has the highest relevance; secondary stresses are not considered directly.

In the existing literature, it is assumed that the primary crack propagates at a characteristic angle of about 45°, relative to the active tooth flank. In case hardened gears the crack starts with a fast growth rate and then slows down towards the component's surface due to the increasing hardness. The crack growth is initially described by fatigue behavior and the associated smooth fracture surfaces and occurring beach marks. After a critical crack length is reached, a force breakage occurs within a few load cycles. In contrast to other tooth flank fatigue damages, a direct failure of the gear stage is associated with the occurrence of flank fracture. (Ref. 22). Figure 17 (right) shows the responsible stresses for flank fractures according to Witzig (Ref. 22).

Compared to pitting damage, stresses in significantly higher depths (approx. a power of ten difference) are crucial. Influences from the friction state and the kinematics are therefore negligible (Ref. 19). Furthermore, the crack initiation location is not in the area of maximum stress, but in the area of lower load capacity (Ref. 20). Therefore, for tooth flank fracture the primary stress caused by the contact pressure, in
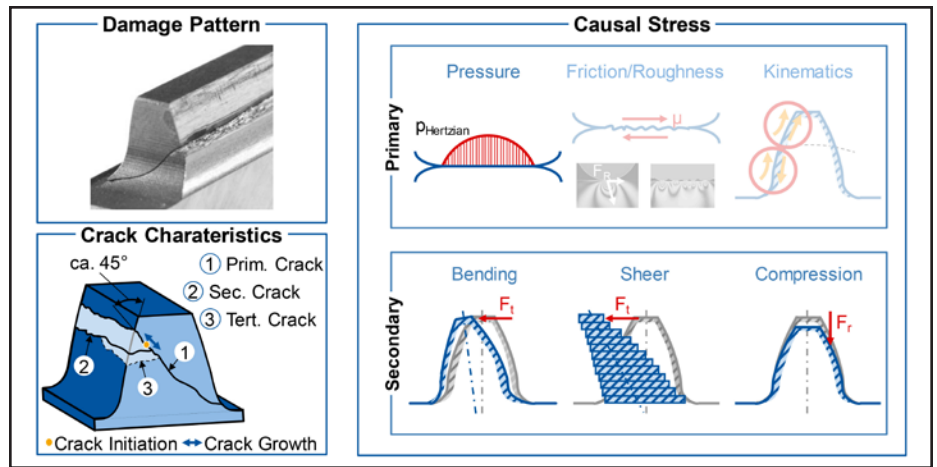


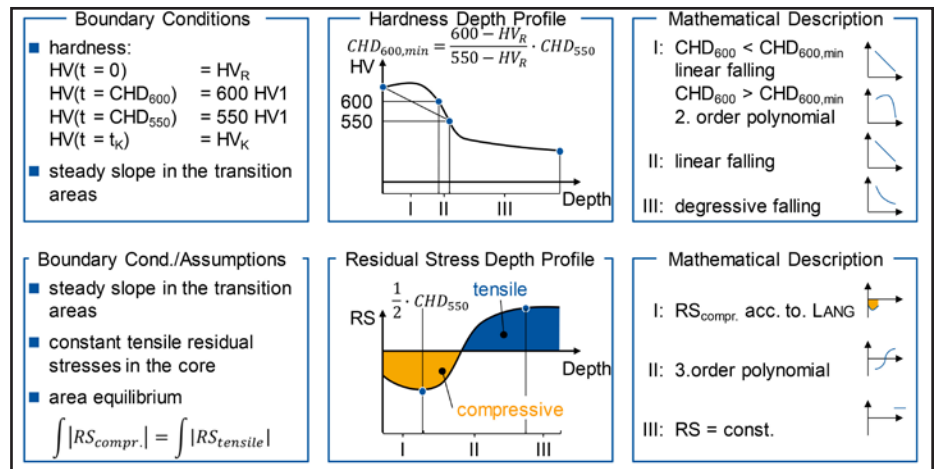Figure 17    Characteristics of tooth flank fracture (Ref. 22).



Figure 18    Calculation of tooth flank fracture load capacity (Ref. 23).

combination with the mechanical secondary stress due to bending, shear and compression, is regarded as causative (Refs. 20 and 22).

In this paper, the calculation of the stress present in the tooth volume is performed according to the approach of Konowalczyk (Ref. 23). The FEA is used in order to achieve the highest possible quality of results. A quasi-static simulation of the gear meshing takes into account the influence of the contact pressure with respect to the primary stress. Influences from the friction and the kinematics are considered subordinate, according to the state of the art and therefore are not considered in the simulation. Furthermore, a simultaneous calculation of the secondary load due to bending, shear and compression takes place. By using the general FEA, all stress components are calculated in their entirety. A superposition of simplified models is not necessary. Furthermore, a 3-D strain state is considered.

The result of the stress calculation is the time-dependent stress tensor for each volume element in the tooth. This represents the input variable for the calculation of an equivalent stress. In order to be able to take into account the characteristic rotation of the main axis system of the rolling contact and the time-dependent stress, the SIH is used for equivalent stress formation in this paper, as demonstrated in the pitting fatigue calculation approach (Refs. 7, 9). In contrast to the work of Witzig, however, not only the maximum value of the shear stress of all sectional planes is considered; but there is a differentiated calculation of an equivalent mean stress and the stress amplitudes. This procedure is carried out once taking into account the load-dependent stresses and once taking into account the residual stresses (Ref. 23).

The hardness and residual stress depths are calculated using analytical formulas based on a few input quantities (Fig. 18). First, the calculation of the hardness depth profile takes place. The

calculation requires the specification of an edge hardness $HV_R$, a core hardness $HV_K$, a case hardening depth $CHD_{550}$ and an additionally introduced case hardening depth $CHD_{600}$. The hardness depth profile is divided into three areas, which are defined by the two specified case hardening depths. The boundary condition for connecting the subdivided areas is a continuous slope in the transition areas. Depending on the surface hardness $HV_R$, the case hardening depth $CHD_{600}$ and the case hardening depth $CHD_{550}$, a minimum case hardening depth $CHD_{600, min}$ is calculated by assuming a linearly decreasing hardness up to the case hardening depth $CHD_{550}$. If the specified case hardening depth $CHD_{600}$ is less than the minimum case hardening depth $CHD_{600,min}$, then the first and second regions are summarized by a linear hardness decline (Ref. 23).

If the specified case hardening depth $CHD_{600}$ is greater than the minimum case hardening depth $CHD_{600,min}$, a hardness depth profile with a hardness plateau is assumed. In this case, the first section of the hardness depth profile up to the case hardening depth $CHD_{600}$ is described by a second-order polynomial. The second section between the two case hardening depths is calculated by a linear function. The third area is described by a degressively decreasing hardness towards the core hardness. By specifying the abovementioned variables and the boundary condition of the continuous slopes in the transition areas, the hardness depth profile is mathematically described. The specification of the introduced second case hardening depth $CHD_{600}$ allows, in contrast to approaches used in the state of the art, the differentiated consideration of a hardness plateau.

The calculation of the residual stress depth curve is divided in sections as well. In the edge area up to half the case hardening depth $CHD_{550}$, the approach according to Lang is used to calculate the residual compressive stresses (Ref. 24). For this depth range, the Lang approach is validated and there are no residual tensile stresses. Subsequently, the estimation of the residual stresses depth profile is carried out via a polynomial of the third order, which describes the transition from the compressive residual stress state into the tensile residual stress section of the residual stress profile. From a certain depth on, constant tensile residual stresses are assumed. The basis for these considerations are the residual stress measurements performed by Witzig using a neutron source (Ref. 22). The amount of residual tensile stresses and the depth at which constant residual tensile stresses are assumed are selected by means of an optimization algorithm in such a way that an equilibrium of compressive and tensile residual stresses results. This approach takes into account the principle of balance forces.

The method for considering defect size and distribution is based on the work of Murakami. This establishes an empirical relationship between the hardness $HV$, the defect area and the alternating strength $\sigma_w$. The method proposed by Murakami has already been extensively validated on simple samples (Ref. 25). Henser successfully used the method in a three-dimensional tooth contact analysis to describe the tooth root load carrying capacity of gears, as demonstrated (Ref. 18). For the representation of the statistical distribution, the calculation of the component's load carrying for flank fracture is also done according to the method of Henser (Ref. 18). In this case a random distribution of imperfections in the tooth volume is generated in successive calculation steps (Fig. 19, top). The random distribution follows a density function of the defects, which results from the degree of purity of the material and is described by the scale parameter $T$ and shape parameter $k$ of a Weibull distribution and a reference number of defects present in the volume. On the basis of the local data regarding the stress, the hardness and the residual stress state, it can be calculated whether a defect causes an exceeding of the local material strength (Fig. 19, bottom-right).

Deviating from the procedure according to Henser, the fatigue strength of a defect is calculated differently in this approach, whereby initially no influence from the locally present mean stresses on the tolerable stress amplitude is considered. This is done in a second step according to the recommendation of Murakami by calculating a mean stress sensitivity (Ref. 25). In this paper the procedure according to FKM is used for the calculation of the mean stress sensitivity (Ref. 12). Since the load-dependent mean stresses are small compared to the residual stresses in the critical region for flank fracture and, furthermore, the sign can be determined for the residual stresses within the SIH only, only the mean stresses resulting from the residual stresses are accounted for.

Based on the strain calculation for each defect in the tooth inner volume, the result of a calculation step is evaluated either as a breakage or as a run out and classified in a simulative stair case method (Fig. 19, bottom left). Based on the result, the load stage for the next step is selected and the load capacity calculation is repeated. The procedure described is repeated a total of 50 times to achieve a high statistical coverage of the result with regard to the mean value and the variance.

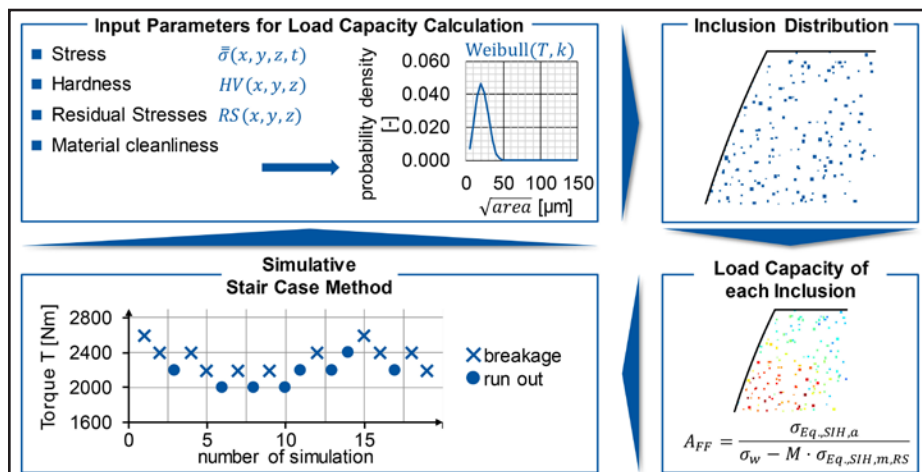First, the simulation was validated using trials from literature (Ref. 22). The



**Figure 19    Method for the consideration of inclusion size and distribution.**

gear chosen was a straight spur gear with a normal module of $mn = 3\,mm$, a number of teeth of $z_{1/2} = 67/69$ and a center distance of $a = 200\,mm$. The material used was the case hardening steel 18CrNiMo7-6 for one variant and the case hardening steel 20MnCr5 for the second variant. The edge hardness $HVR$, the case hardening depths $CHD600$ and $CHD550$ and the core hardness $HVK$ are shown in Figure 20. Since the inclusion distribution for the given material batch was not available in the publication, a synthetic distribution based on experimental data of a different batch of the same material and on data collection from the pictures in the publication was used. The resulting torque level for a probability of failure of 50% for the test bench trials, the FE-simulation and the ISO/DTS 6336-4 calculation are shown in the upper half of Figure 20. In this case, both the ISO calculation as well was the FE approach match the test bench results with minor deviations. In the lower half, the strain depth profile is plotted and compared to the depth where crack initiation areas were identified. The critical strain for the occurrence of flank breakage is set to $A = 0.8$ for the ISO calculation and $A = 1.0$ for the FE approach. Both methods predict flank fracture correctly and show the strain maxima in the depth where the crack initiation took place. The ISO calculation as well as the FE-simulation tend to predict the critical depth to be on the lower side, with the FE-simulation being more precise for the given case.

To validate the FE simulation with a second gear geometry a straight spur gear with a normal module of $mn = 8\,mm$, a number of teeth of $z_{1/2} = 24/25$ and a center distance of $a = 200\,mm$ was chosen. The material used was the case hardening steel 18CrNiMo7-6. The edge hardness $HVR$, the case hardening depths $CHD600$ and $CHD550$ and the core hardness $HVK$ are listed (Fig. 21). The calculations of the fatigue strengths were again performed according ISO/DTS 6336-4 as well as according to the FE-approach described in this paper and both are compared to test bench results. The results demonstrate that the FE-based model is clearly more accurate than the approach according to ISO/DTS
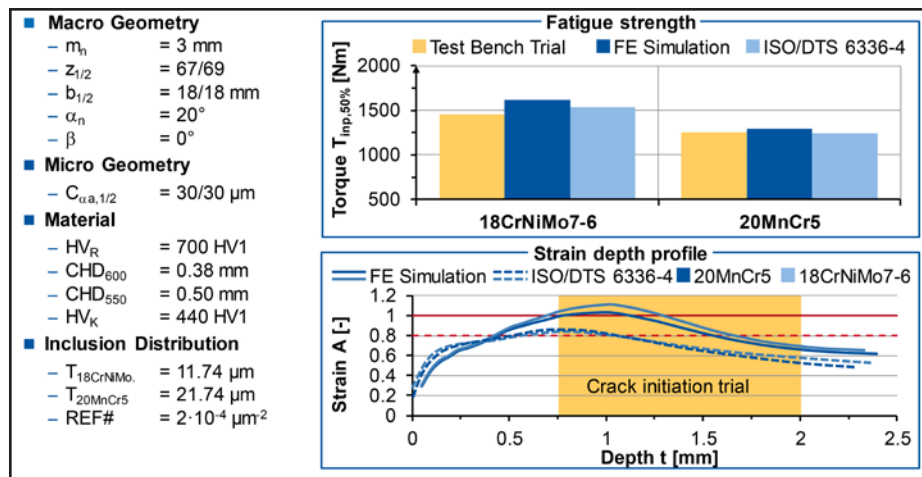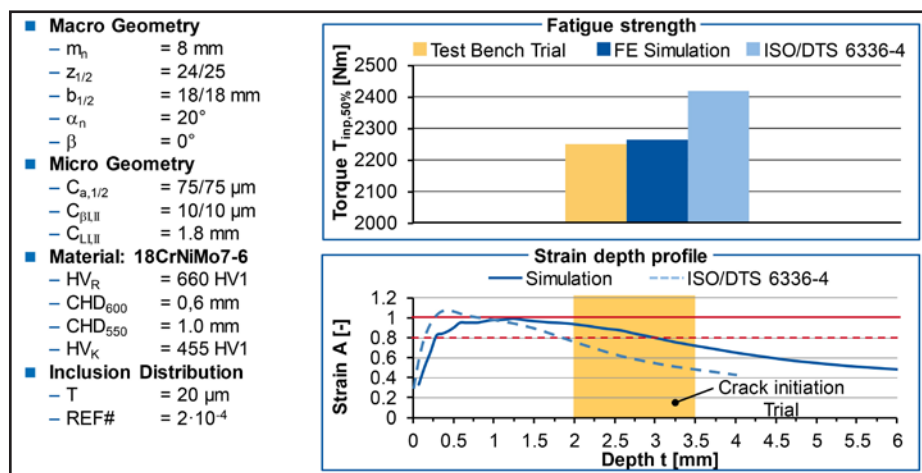


Figure 20    Method validation module 3 mm.



Figure 21    Method validation module 8 mm.

6336-4. The calculation of the strain in the gear according to ISO/DTS 6336-4 shows the highest strain near the surface, Figure 21, lower half. The strain then stays on a high level until a depth of $t = 1.25\,mm$ is reached. After that, the strain steadily decreases over the depth. The flank fractures occurred during testing had their crack initiation site in depths of $t = 2.0... 3.5\,mm$. Thus, on the one hand, a flank breakage probability is shown by means of the calculation model. On the other hand, the depth of the highest strain does not agree with the test bench results. The same is true for the FE-based approach in terms of the strain prediction.

Although the prediction of the highest strain is closer to the crack initiation area in the FE-based approach compared to the model of ISO/DTS 6336-4, it also shows a lower critical depth by trend. Both approaches should be optimized in the future to improve the prediction of the crack initiation depth for

arbitrary gear geometries.

## Summary and Outlook

Power density is a key factor in gear design. Increasing the power density enables engineers to use smaller gears for their applications which lead to smaller and lighter gear boxes. The required high power density of the gearbox demands an exact calculation method for the strength against the predominant failure modes of the given gear sets. This includes pitting, tooth root breakage and flank fracture. The precise recalculation of the tooth strength is necessary, as the downsizing leads to a reduction of the remaining safety reserves.

With regards to the calculation of the strength of cylindrical gears a trend towards local calculation approaches is visible. Instead of calculations solely based on standards and global calculation approaches, local approaches based on Finite Element Analysis (FEA) are used. It was demonstrated in this paper,

how FE-based models can be used to predict the most common failure modes pitting, tooth root breakage and flank fracture for a 50% probability of failure.

The prediction of the fatigue strength for pitting and tooth root breakage by the FE-based methods was very accurate for all geometries shown in this paper. It was demonstrated how the ISO standard became very inconsistent with the test bench results when the scope of the standard was exceeded, although the geometries investigated were not uncommon in the gear industry. In contrast to the standard, the accuracy of local FE-based approaches is not directly affected by the gear geometry by design.

For flank fracture the results were not as good as for pitting or tooth root breakage. This is true for the ISO/DTS 6336-4 as well as the FE-approach. Flank fracture has its origin in the inner material volume which increases the difficulty of correctly describing the stress state. For example, there is no viable option to measure the residual stresses in that area. Therefore, more assumptions are used to predict those characteristics. More research needs to go into improving the FE-based calculation methods for flank fracture in particular. Additionally, the validity for a 1% probability of failure needs to be proven.

An additional benefit of the local approaches is the direct consideration of the cleanliness of the steel, which was not targeted in particular in this paper. The downside of the FE-approaches is that the material needs to be characterized well to achieve consistent results. But without material characterization there is no way to achieve the maximum power density independent from the chosen approach. For non-critical low load applications, FE-based methods can offer a tool to predict minimum steel cleanliness in favor to achieve a cost benefit. **PTE**

## References

1.  Braykoff, C., 2007, "Tragfähigkeit kleinmoduliger Zahnräder", Ph.D. thesis, Technical University of Munich.
2.  Grzybowski, R. and Steingröver, K., 2007, "Das Getriebe für Windkraftanlagen im Fokus der nationalen und internationalen Normung", *Dresdner Maschinenelement Kolloquium*, Dresden.
3.  International Organization for Standardization (ISO), 2007, "Calculation of load capacity of spur and helical gears," ISO 6336-2.
4.  International Organization for Standardization (ISO), 2007, "Calculation of load capacity of spur and helical gears," ISO 6336-3.
5.  American Gear Manufacturing Association (AGMA), 2001, "Fundamental Rating Factors and Calculation Methods for Involute Spur and Helical Gear Teeth", ANSI/AGMA 2001-D04.
6.  International Organization for Standardization (ISO), 2017, "Calculation of load capacity of spur and helical gears," ISO/DTS 6336-4.
7.  Löpenhaus, C., 2015, "Untersuchung und Berechnung der Wälzfestigkeit im Scheiben- und Zahnflankenkontakt", Ph.D. thesis, RWTH Aachen University.
8.  Hertter, T., 2003, "Rechnerischer Festigkeitsnachweis der Ermüdungstragfähigkeit vergüteter und einsatzgehärteter Stirnräder", Ph.D. thesis, Technical University of Munich.
9.  Liu, J., 1991, "Beitrag zur Verbesserung der Dauerfestigkeitsberechnung bei mehrachsiger
10. Beanspruchung", Ph.D. thesis, Technical University of Clausthal. Klubberg, F., Schäfer, H. J., Hempen, M. and Beiss, P., 2001; "Mittelspannungsempfindlichkeit metallischer Werkstoffe bei schngender Beanspruchung", *Roell Amsler Symposium „World of Dynamic Testing"*, Gotmading, pp.111–134.
11. Winderlich, B., 1990, "Das Konzept der lokalen Dauerfestigkeit und seine Anwendung auf martensitische Randschichten, insbesondere Laserhärtungsschichten", Materialwissenschaften und Werkstofftechnik, 21, pp.378–389.
12. Forschungskuratorium Maschinenbau e.V., 2003, "Rechnerischer Festigkeitsnachweis für Maschinenbauteile", 5th ed., VDMA Verlag, Frankfurt a.M.
13. Haibach, E., 2006, "Betriebsfestigkeit. Verfahren und Daten zur Bauteilberechnung.", 3rd ed., Springer, Berlin.
14. Brecher, C., Brumm, M. and Löpenhaus,C., 2014, "Improvements in Manufacturing Related Surfae Strength Increase and Rolling Contact Fatigue Simulation", *WZL Gear Conference USA*, Rochester, pp.15-1–15-25.
15. Brecher, C., Renkens, D. and Löpenhaus, C., 2016, "Method for Calculating Normal Pressure Distribution of High Resolution and Large Contact Area", ASME Journal of Tribology, 138.
16. Bugiel, C., 2009, "Tribologisches Verhalten und Tragfähigkeit PVD-beschichteter Getriebe-Zahnflanken", Ph.D. thesis, RWTH Aachen University.
17. Tobie, T., 2001, "Zur Grübchen- und Zahnfußtragfähigkeit einsatzgehärteter Zahnräder. Einflüsse aus Einsatzhärtungstiefe, Wärmebehandlung und Fertigung bei unterschiedlicher Baugröße", Ph.D. thesis, Technical University of Munich.

## For more information.

Have questions or comments regarding this technical paper? Contact WZL's Dr. Christoph Löpenhaus at *c.loepenhaus@wzl.rwth-aachen.de.*

**Dr. Marco Kampka** is a 2012 graduate of RWTH Aachen University, having studied mechanical engineering with a focus on production engineering. He began his career working in 2012 as a scientific research assistant at the gear department of the Laboratory of Machine Tools and Production Engineering (WZL). In July 2017, he finished his doctoral thesis and joined Fraunhofer CMI in Boston, MA as the head of the gear and transmission technology group. Today, Dr. Kampka is a technical sales manager at Gleason-Pfauter Maschinenfabrik GmbH in Ludwigsburg, Germany.

**Prof. Dr.-Ing. Christian Brecher** has since January 2004 been Ordinary Professor for Machine Tools at the Laboratory for Machine Tools and Production Engineering (WZL) of the RWTH Aachen, as well as Director of the Department for Production Machines at the Fraunhofer Institute for Production Technology IPT. Upon finishing his academic studies in mechanical engineering, Brecher started his professional career first as a research assistant and later as team leader in the department for machine investigation and evaluation at the WZL. From 1999 to April 2001, he was responsible for the department of machine tools in his capacity as a Senior Engineer. After a short spell as a consultant in the aviation industry, Professor Brecher was appointed in August 2001 as the Director for Development at the DS Technologie Werkzeugmaschinenbau GmbH, Mönchengladbach, where he was responsible for construction and development until December 2003. Brecher has received numerous honors and awards, including the Springorum Commemorative Coin; the Borchers Medal of the RWTH Aachen; the Scholarship Award of the Association of German Tool Manufacturers (Verein Deutscher Werkzeugmaschinenfabriken VDW); and the Otto Kienzle Memorial Coin of the Scientific Society for Production Technology (Wissenschaftliche Gesellschaft für Produktionstechnik WGP).

**Dr. -Ing. Dipl. -Wirt. -Ing. Christoph Löpenhaus** has since 2014 served as Chief Engineer in the Gear Department of WZL, RWTH Aachen / Laboratory of Machine Tools and Production Engineering (WZL), RWTH Aachen. He previously held positions there as (2011–2014) Team Leader, Group Gear Testing Gear Department Chair of Machine Tools Laboratory of Machine Tools and Production Engineering (WZL) RWTH Aachen; (2010–2011) Research Assistant, Group Gear Testing Gear Department Chair of Machine Tools Laboratory of Machine Tools and Production Engineering (WZL) RWTH Aachen: (2007–2009) as Student Researcher, Group Gear Design and Manufacturing Calculation Gear Department Chair of Machine Tools Laboratory of Machine Tools and Production Engineering (WZL) RWTH Aachen; and (2004–2009) as a student in Industrial Engineering RWTH Aachen.